Synthesis and Characteristics of Transferrable Single-Crystalline AlN Nano-membranes

Jiarui Gong[1,2,†], Jie Zhou[2,†], Ping Wang[3,†], Tae-Hyeon Kim[4], Kuangye Lu[5], Seunghwan Min[2], Ranveer Singh[2], Moheb Sheikhi[2], Haris Naeem Abbasi[2], Daniel Vincent[2], Ding Wang[3], Neil Campbell[1], Timothy Grotjohn[6], Mark Rzchowski[1], Jeehwan Kim[5], Edward T. Yu[4,], Zetian Mi[3,*], and Zhenqiang Ma[2,*]*

Jiarui Gong, Neil Campbell, Mark Rzchowski
[1]Department of Physics, University of Wisconsin-Madison, Madison, Wisconsin, 53706, USA

Jiarui Gong, Jie Zhou, Seunghwan Min, Ranveer Singh, Moheb Sheikhi, Haris Naeem Abbasi, Daniel Vincent, Zhenqiang Ma
[2]Department of Electrical and Computer Engineering, University of Wisconsin-Madison, Madison, Wisconsin, 53706, USA
Email: mazq@engr.wisc.edu

Ping Wang, Ding Wang, Zetian Mi
[3]Department of Electrical Engineering and Computer Science, University of Michigan, Ann Arbor, Michigan, 48109, USA
Email: ztmi@umich.edu

Tae-Hyeon Kim, Edward T. Yu
[4]Microelectronics Research Center, Department of Electrical Engineering and Computer Science, University of Texas at Austin, Austin, Texas, 78758, USA
Email: ety@ece.utexas.edu

Kuangye Lu, Jeehwan Kim
[5]Department of Mechanical Engineering, Department of Materials Science and Engineering, Massachusetts Institute of Technology, Cambridge, Massachusetts, 02139, USA

Timothy Grotjohn
[6]Department of Electrical and Computer Engineering, Michigan State University, East Lansing, Michigan, 48824, USA

[†]These authors contributed equally to this work.
[*]Author to whom correspondence should be addressed. Electronic mail: mazq@engr.wisc.edu, ztmi@umich.edu, ety@ece.utexas.edu

Author Manuscript

This is the author manuscript accepted for publication and has undergone full peer review but has not been through the copyediting, typesetting, pagination and proofreading process, which may lead to differences between this version and the Version of Record. Please cite this article as doi: 10.1002/aelm.202201309.

This article is protected by copyright. All rights reserved.

Abstract

Single-crystalline inorganic semiconductor nano-membranes (NMs) have attracted great attention over the last decade, which poses great advantages to complex device integration. Applications in heterogeneous electronics and flexible electronics have been demonstrated with various semiconductor nanomembranes. Single-crystalline aluminum nitride (AlN), as an ultrawide-bandgap semiconductor with great potential in applications such as high-power electronics has not been demonstrated in its NM forms. In this very first report, we demonstrate the creation, transfer-printing, and characteristics of the high-quality single-crystalline AlN NMs. We successfully transferred the AlN NMs onto various foreign substrates. The crystalline quality of the NMs has been characterized by a broad range of techniques before and after the transfer-printing and no degradation in crystal quality has been observed. Interestingly, a partial relaxation of the tensile stress has been observed when comparing the original as-grown AlN epi and the transferred AlN NMs. In addition, the transferred AlN NMs exhibits the presence of piezoelectricity at the nanoscale, as confirmed by piezoelectric force microscopy. We also commented on the advantages and the challenges of our approach. Potentially, the novel approach opens a viable path for the development of the AlN-based heterogeneous integration and future novel electronics and optoelectronics.

Keywords: AlN, single-crystalline nano-membrane, transfer-printing, scanning transmission electron microscopy, piezoresponse force microscopy, X-ray photoelectron spectroscopy, UWBG

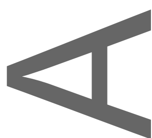

This article is protected by copyright. All rights reserved.

1. Introduction

Single-crystalline inorganic semiconductor nano-membranes (NMs), which have a thickness of less than a few hundred nanometers, have gained increasing interest since 2005 due to their remarkable use for a variety of applications. These free-standing NMs can be transferred to any arbitrary foreign substrates by using elastomeric stamps, which was first demonstrated by Meitl *et al*.. [1] Importantly, these NMs are compatible with the traditional semiconductor manufacture approach for fabricating various heterogeneously integrated and flexible electronic devices, [2-4] including the seamless integration of semiconductor NMs with the low-cost, CMOS-compatible silicon (Si) substrates. Until now, several applications of transferrable monocrystalline NMs based on Si, [4-20] germanium (Ge), [4, 21] gallium arsenide (GaAs)/aluminum gallium arsenide (AlGaAs), [4, 22-26] gallium nitride (GaN)/aluminum gallium nitride (AlGaN), [27-30] silicon carbide (SiC), [31] gallium oxide (Ga_2O_3), [32-35] etc. have been reported during the last few years. These transferrable narrow, wide, and ultrawide bandgap NMs have enabled a variety of device applications over the past nearly two decades.

In comparison to the above semiconductors that have been released in the form of NMs, single-crystalline aluminum nitride (AlN) has the unique properties of ultrawide direct bandgap (6.2 eV), [36] high breakdown electric field (15.4 MV/cm), [37] good thermal conductivity (3.19 W/cmK), [38] strong spontaneous polarization, and good piezoelectricity. These properties enable AlN for applications in ultraviolet (UV) wavelength sensing, [39, 40] power electronics, [41, 42] piezoelectric devices, [43-48] etc. Furthermore, the polarization properties of single-crystalline AlN can induce free charges at the heterointerface and influence mobile carrier distributions via polarization-induced bound charges, an approach which is expected to be much more effective than doping via impurities. [49] Previously, several attempts have been made to grow and release the high-quality free-standing AlN NMs. For instance, Y. Mei *et al*. used metal-organic vapor phase epitaxy (MOVPE) to grow

This article is protected by copyright. All rights reserved.

porous crystalline AlN/GaN thin films over the Si (111) substrate and further, released it by selective Si wet etching.[50] In another report, J. Yang *et al*. sputtered polycrystalline AlN on the silicon dioxide (SiO_2) substrate by magnetron sputtering and released the NMs through selective SiO_2 wet etching.[51] Recently, AlN thin film was grown on Ge and Si substrates by radio frequency (RF) magnetron reactive sputtering and molecular beam epitaxy (MBE), respectively, which was released by selective gas-phase dry etching of Ge and Si.[52, 53] However, these AlN materials were not transferred to a foreign semiconductor substrate, which greatly limits their potential applications. Thus, it is very important not only to fabricate the electronic devices but also from a fundamental point of view to carry out a detailed study on the transfer of free-standing AlN NMs.

A few studies on transferring AlN thin films to flexible adhesive substrates have been reported recently.[54-56] However, there exist three issues: 1) the AlN crystalline quality, e.g., grain size, crystal orientation, in the above-mentioned studies is rather low due to the growing methods, which are limited by the growth approaches; 2) the adhesive handling materials during the transfer can leave residues on the AlN film; 3) only adhesive flexible substrates have been demonstrated as the final host substrate, which eliminate the potential of applications such as AlN-based vertical devices.[4] Hence, it is desirable to overcome the above issues and achieve a high-quality transferrable single-crystalline AlN NM that can be transferred to a broader range of substrates.

In this work, we demonstrate the synthesis and characterizations of the transferrable single-crystalline AlN NMs. We have successfully transferred the AlN NMs onto flat sapphire, flat Si, and pillar-structured Si substrates. The crystal features are characterized by X-ray diffraction (XRD), Raman spectroscopy, and scanning transmission electron microscope (STEM) techniques. Importantly, no degradation has been observed in the crystallinity of the AlN NMs before and after transfer on the different substrates, highlighting

This article is protected by copyright. All rights reserved.

the quality of the transferred NMs. Further, atomic force microscopy (AFM) is employed to monitor the surface roughness of as-grown Al-polar and post-transferred N-polar AlN NMs, confirming the ultra-smooth surface of the NMs. Piezoresponse force microscopy (PFM) confirms the presence of the piezoelectricity in the transferred AlN NMs. X-ray photoelectron spectroscopy (XPS) was employed to characterize the valence band maximum (VBM) on both Al-polar and N-polar surfaces, without and with various atomic-layer-deposited (ALD) ultrathin oxide (UO) coatings. Based on the above experimental results, the present study not only opens a new insight for the fundamental device fabrication but also provides a novel platform for a broad range of electronic, optoelectronic, and photonic device applications.

2. Results and discussion

Author Ma

This article is protected by copyright. All rights reserved.

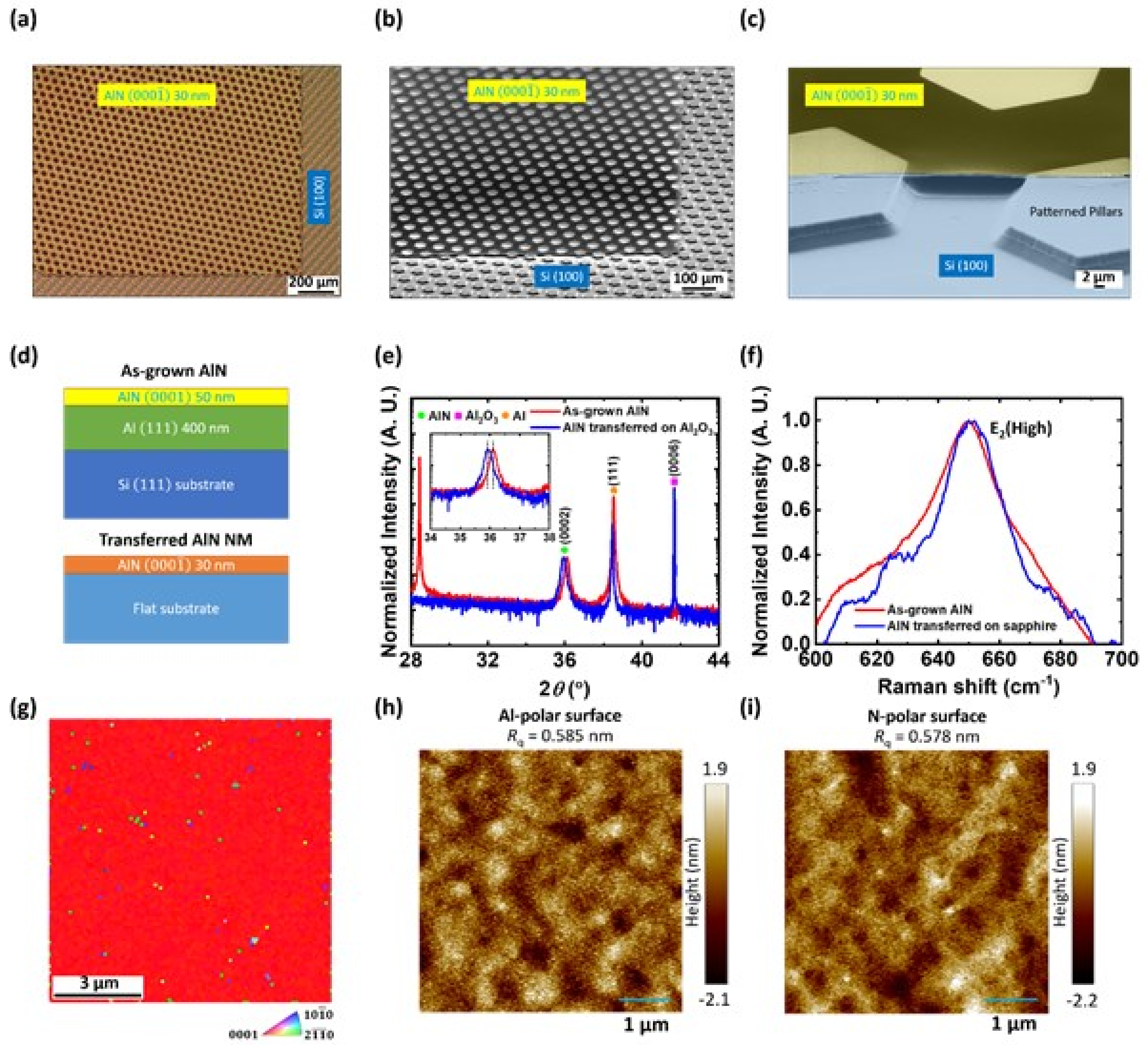

Figure 1. (a) Optical image (a top view) and (b, c) SEM images (tilted views) of single-crystalline AlN NM transferred on a Si (100) substrate that has an array of patterned hexagon shaped pillars. (d) Schematics of the AlN (0001)/Al (111)/Si (111) epi wafer (top) and the AlN (000$\bar{1}$) NM transferred onto the flat substrate (bottom). (e) XRD 2theta-omega scans and (f) Raman spectra of the as-grown AlN epi and the transferred AlN NM on sapphire (0001) substrate. XRD peaks of Si (111), AlN (0002), Al (111), and Al_2O_3 (0006) planes are observed and labeled in (e). The inset of (e) shows the enlarged spectra around the AlN (0002) peaks. AlN E_2(high) Raman peak is observed and labeled in (f). (g) EBSD map of the transferred AlN NM on the flat Si substrate. (h) (i) The AFM images of (h) Al-polar surface

This article is protected by copyright. All rights reserved.

(as-grown) and (i) N-polar surface (post-transferred AlN NM on the Si (100) substrate) of the single-crystalline AlN NM. The surface roughness is about the same for both surfaces.

Initially, the AlN layer was grown using MBE and further, it was successfully transferred onto a flat sapphire (Figure S1), a flat Si (Figure 2(a), (b) and Figure 3(a)), and a hexagon pillar-structured Si (Figure 1(a)-(c)) substrates. Figure 1(a) exhibits the optical image of the transferred AlN NMs on the pillar-structured Si substrate. The pillar-structured Si substrate was prepared via photolithography and RIE and the height of the pillars is about 4 µm. The pillars can be seen through the AlN NM due to the high optical transparency of AlN. Figure 1(b) and (c) present the tilt-view SEM images of transferred AlN NMs on the pillar-structured Si substrate. These SEM images clearly confirm the uniformity of the NMs over the whole substrate without formation of cracks. The high-resolution SEM image (Figure 1(c)) confirms the smoothness of the NMs edges, which are highly desired from the device fabrication point of view. It is noted from Figure 1(c) that the AlN NM has sufficient rigidity even with a thickness of only 30 nm (Figure 2(a)). The schematics of as-grown AlN and transferred AlN on flat Si substrate have been illustrated in Figure 1(d).

A desirable feature to use NMs for device fabrication is to have great crystalline quality and it is well-known that the crystallinity of a layer strongly depends on the growth process. Therefore, XRD measurements are performed to study the crystalline quality of the AlN NMs before and after the transfer-printing process. 2theta-omega spectra of the epi wafer and AlN NM transferred on the sapphire (0001) substrate were characterized. Figure 1(e) shows the XRD pattern of the AlN epi sample and the transferred AlN on sapphire sample. Of note, the spectrum of the AlN epi sample was aligned by the Si (111) peak while the one of the transferred AlN NM sample was aligned by the Al_2O_3 (0006) peak during the XRD measurement. From Figure 1(e), it is evident that both the samples are high crystalline in nature and the AlN (0002) peak are found to be located at 36.11° and 35.92°. The decrease

This article is protected by copyright. All rights reserved.

in the 2θ (as is seen from the inset of Figure 1(e)) indicates the increase of the interplane spacing d in the corresponding direction, i.e., AlN (0002), according to the Bragg condition:

$$n\lambda = 2d \sin\theta, \tag{1}$$

where n is the diffraction order and λ is the wavelength. In addition, the measured full width at half maximums (FWHM) of the AlN (0002) peaks from the AlN epi sample and the transferred AlN on sapphire sample are 0.210° and 0.216°, respectively, indicating no significant degradation of the AlN crystalline quality throughout the transfer process. Further, the crystallite size can be calculated using the Scherrer equation [57, 58]

$$L = \frac{K\lambda}{\beta \cos\theta}, \tag{2}$$

where L is the average size of the crystallite domains, K is the shape factor (which is taken as 1 for estimation), λ is the wavelength of the X-ray (1.5418 Å), β is the FWHM in radians, and θ is the Bragg angle. The estimated crystallite size of the transferred AlN NMs is found to be ~44 nm. The obtained value of crystallite size is better than the ones of the AlN thin films transferred on the flexible substrates. [55, 56] It is further noticed that the grain size is mainly limited by the epi film thickness (50 nm). In Figure 1(e), the peak observed at 2θ = 38.46° in the XRD spectrum of the transferred AlN on sapphire sample is related to the Al residue after plasma etching (Figure S1). As mentioned in the experiment section, the exposure of the AlN in the transparent region has been confirmed by XPS survey scan (Figure S2).

To obtain more details on the crystalline structure, the EBSD map is collected on the transferred AlN NM as shown in Figure 1(g). The map shows (0001) in-plane orientation (red region), which matches the results from XRD spectra (Figure 1(e)). Some isolated points

This article is protected by copyright. All rights reserved.

with other colors are likely due to the low signal-to-noise ratio for this 50 nm AlN NM during the EBSD measurement in SEM and mistakenly generated by the fitting software.

Further, for in-depth study about vibrational properties, the micro-Raman measurements are carried out on the as-grown and transferred AlN NMs to confirm the formation of AlN and measure the stress inside the NMs. It has been confirmed that no major peaks were located between 650 cm^{-1} and 660 cm^{-1} from the spectra of the Al and the sapphire substrates (Figure S3). As shown in Figure 1(f), the Raman shift appearing at 650 cm^{-1} on the epi sample and 651 cm^{-1} on the transferred AlN NMs on the sapphire substrate is associated to the E_2 (high) Raman mode of AlN, which corresponds to a biaxial tensile stress of 1.17 GPa and 1.02 GPa, respectively. [59] The existence of tensile stress aligns with the curling phenomenon observed during the transfer-printing process, as described in the experiment section. In addition, no significant change has been observed in the Raman spectra of AlN NMs before and after the transfer-printing process, confirming the high quality of the transferred AlN NMs. The measured FWHM of the E_2(high) peak is 34 cm^{-1} for the AlN epi sample and 26 cm^{-1} for the AlN transferred on sapphire sample. The decrease in the FWHM of the E_2(high) peak after the Al removal indicates the partial relaxation of the stress gradient in the AlN NMs, [60] which also agrees well with the Raman E_2(high) peak shift and the XRD AlN (0002) peak shift.

It is well-known that a smooth interface is highly desirable to fabricate the high performing electronic devices. Therefore, the surface roughness of the AlN NMs has been measured from both sides by AFM. Figure 1(h) and (i) depict the morphological images of AlN epi sample (Al-polar surface) and transferred AlN NMs (N-polar surface), respectively. It is interesting to note that the AlN NMs from both the polarities show a smooth surface having root mean square (RMS) of 0.585 and 0.578 nm. After transferring the AlN NMs (N-

This article is protected by copyright. All rights reserved.

polar surface), the RMS is found to be comparable to that of Al-polar surface even with plasma etching process of Al layer.

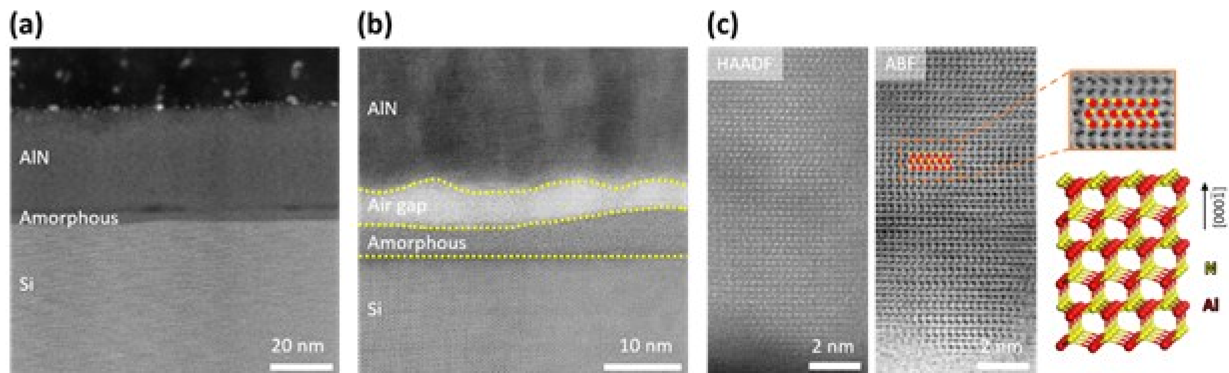

Figure 2. Microstructural analysis of the transferred AlN NM. (a) Cross-sectional HAADF-STEM image of the transferred AlN NM on the Si (100) substrate. The AlN layer thickness is 30 nm. (b) ABF-STEM image of the interface between the AlN NM and the Si (100) substrate. A local air gap was observed. (c) High resolution HAADF-STEM image (left) and the corresponding ABF-STEM image (right) of the AlN membrane. Al atoms (the red balls) and N atoms (the yellow balls) are embedded in (c) to visualize the atomic stacking sequence, showing a clear N-polar lattice. Reconstructed atomic structure from the STEM images is shown in the bottom right of (c).

To understand the micro-structural and crystalline nature of the transferred AlN NMs, cross-sectional HAADF-STEM technique was employed. The sample was an AlN NM transferred onto a Si substrate that was coated with amorphous Al_2O_3 using atomic layer deposition (ALD). The ALD-Al_2O_3 coating was to mimic the situation of the grafted heterostructures. [4] The sample was annealed at 350 °C for 5 min in N_2 ambient via rapid thermal annealing (RTA) after the NM transfer-printing to achieve chemical bonding between the NM and Si substrate. Figure 2(a) shows the cross-sectional HAADF-STEM image of the transferred AlN membrane on the Si substrate, which not only confirms the uniformity of the AlN NMs but also reveals the thickness of the NMs (~30 nm). Importantly,

This article is protected by copyright. All rights reserved.

no other defects, damages, stacking faults, or threading dislocations were observed in the transferred AlN NMs, confirming the high quality of the NMs. And the top Al layer was removed completely during the excess dry etching process. Originally, the thickness of the AlN layer is 50 nm whereas after transferring it is found to be 30 nm. The thickness of AlN layer decreases because of the aggressive plasma etching process (as shown in Figure 5(h)).

Figure 2(b) shows an amorphous layer between the AlN membrane and Si substrate, as marked by yellow dotted lines in Figure 2(b). Even though we had removed the native oxide of the Si substrate by HF solution before the ALD-Al_2O_3 deposition, the sample was unavoidably exposed to air before it was sent into the ALD chamber, resulting in the formation of Si native oxide over the Si substrate.[20, 61] Furthermore, the sample underwent the RTA process after the NM transfer, which may induce oxygen diffusion from the interface into the substrate and thus the formation of Si native oxide.[20] Therefore, the amorphous layer is expected to consist of both ALD-Al_2O_3 and Si native oxide (SiO_x). In addition, we also observed an air gap locally in some regions between the substrate and the transferred AlN NM. It is speculated that the local air gaps were generated due to the rigidity/stiffness of the AlN NM,[62, 63] which caused its non-intimate contacts with the substrate at various locations. The RTA process can exacerbate the air gaps due to the large mismatch of thermal expansion coefficients between Si and AlN.[64] Figure 2(c) presents the high-resolution HAADF-STEM image and the corresponding ABF-STEM image acquired from the transferred AlN membrane. From Figure 2(c), it is found that the transferred AlN NMs is highly crystalline and has a highly ordered wurtzite lattice without in-plane rotation or cubic phase, agreeing well with the XRD results. It is well known that in the ABF-STEM image, the darkest spots correspond to the heaviest atoms.[65, 66] Therefore, we are able to configure the atomic stacking sequence of Al and N atoms, which is embedded in the ABF-STEM image (Figure 2(c)). Comparing with the atomic structure of wurtzite AlN, we

This article is protected by copyright. All rights reserved.

confirmed that the lattice-polarity of the transferred AlN membrane is N-polar. In other words, the as-grown AlN on Al/Si template has an Al-polar lattice. These results unambiguously confirm that the transferred AlN membrane has a single-crystalline wurtzite phase with a N-polar lattice.

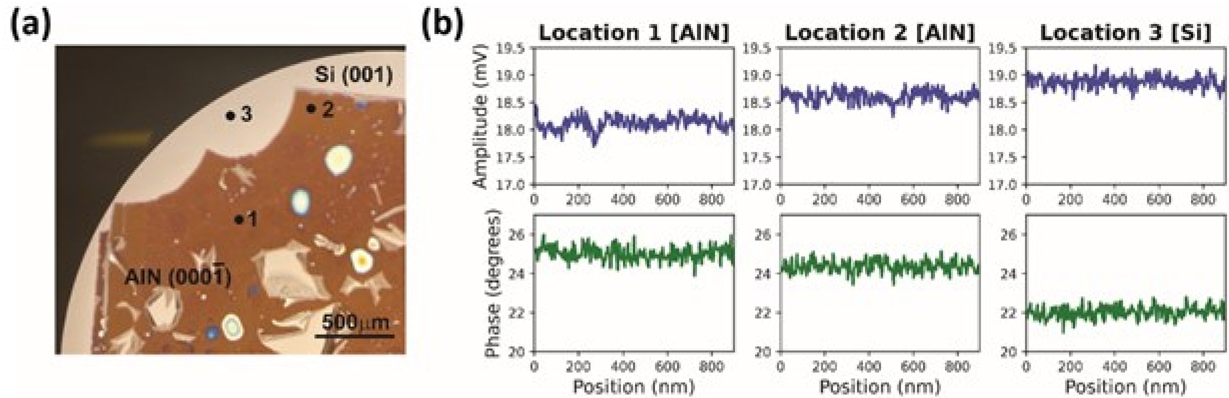

Figure 3. (a) Photograph of AlN/Si sample and location for which PFM measurements are shown. Darker regions correspond to the AlN $(000\bar{1})$ thin film, and light regions to the Si (001) substrate. (b) Amplitude (blue lines, top) and phase (green lines, bottom) of surface modulation measured during PFM measurement. Locations 1-3 are indicated in (a).

The intrinsic polarization in III-nitride semiconductors plays an important role to fabricate the high electron mobility or high hole mobility devices. Therefore, the piezoelectric response of the transferred AlN $(000\bar{1})$ NMs on the flat Si (001) substrate, according to the conductivity requirement for the substrate, was confirmed using PFM.

Figure 3(a) shows a digital photograph of an AlN $(000\bar{1})$/Si (001) sample which was used to characterize the piezoelectric response. As shown in Figure 3(a), the dark brown region and bright region correspond to the AlN NM and Si substrate, respectively. The colorful features shown in the optical image of Figure 3(a) are explained in details in the supplementary information (SI) (Figure S4). For PFM measurement, the sample was annealed at 350 °C for 5 min in N_2 ambient via RTA to ensure good contact between the AlN

This article is protected by copyright. All rights reserved.

NM and the Si substrate. In Figure 3(a), three different locations on the sample were marked, from which the PFM amplitude and phase data were obtained. Locations 1 and 2 were situated on the AlN layer, while location 3 was on the Si substrate, for which no piezoelectric response should be present. PFM measurements were also performed at several other locations on both the AlN NM and Si substrate to confirm their uniformity, and the results obtained are very similar to those shown in Figure 3(b). Figure 3(b) shows the amplitude and phase of surface modulation induced by applied bias voltages V_{dc} = 0 V and V_{ac} = 4 V at locations 1-3 indicated in Figure 3(a). The electromechanical response associated specifically with the AlN NM layer was then determined using a background subtraction approach, described in detail elsewhere, [67, 68] with the PFM measurements performed using values for V_{dc} and V_{ac} of 0-4 V and 3-5 V, respectively, at a frequency of 60 kHz. Negligible variation in measurement results were observed over these ranges of voltages and across multiple samples. The resulting value of $|d_{33,eff}|$ for the AlN NM was found to be 0.65 ± 0.12 pm/V. We assume based on STEM results reported here (Figure 2) that the AlN NM after transfer is N-polar; because of parasitic tip-sample capacitance effects, [69] the polarity of the nanomembrane cannot be determined definitively from these PFM measurements. We can then correct for the deformation of the Si substrate during the PFM measurement using the analysis in the reference, [70] values for the Young's modulus of AlN and Si of 340 GPa and 170 GPa, respectively, and Poisson's ratio of AlN and Si of 0.25 and 0.27, respectively. [71-73] The resulting value for $|d_{33}|$ of the AlN NM ($|d_{33(AlN)}|$) was = 5.2 ± 1.1 pm/V, in excellent agreement with values reported in the literature of 5.0-5.6 pm/V. [74-76]

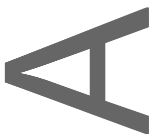

This article is protected by copyright. All rights reserved.

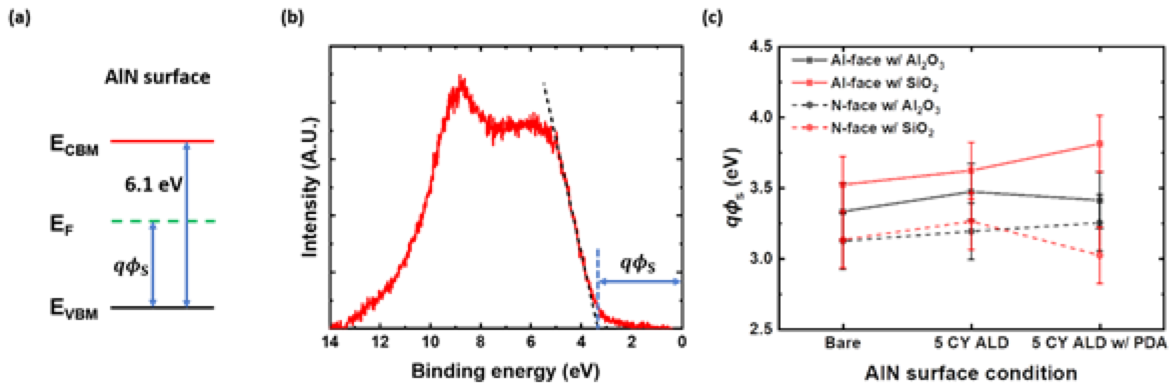

Figure 4. (a) Schematic band diagram at the surface of AlN. (b) An example of AlN valence band XPS spectrum. The black dash line is the linear fitting curve to extract the value of $q\phi_S$ as shown in the graph. (c) The summary of $q\phi_S$ measured on both Al-polar (solid) and N-polar (dash) surfaces, with ultrathin ALD-Al_2O_3 (black) or ALD-SiO_2 (red) coating.

The bandgap of AlN has been reported to be ~6.1 eV by measuring the optical absorption spectra (Tauc plot) and photoluminescence (PL) spectra. [77, 78] Further, to construct the energy band diagram and explore the surface charge states, the VBM using the XPS measurements was calculated on both Al-polar and N-polar, as shown in Figure 4(a). The charge correction was conducted using the C 1*s* peak at 284.6 eV [79] and a Shirley background [80] was subtracted. The energy difference between the VBM and Fermi level, $q\phi_S$, was extracted as the X-intercept of the linear fitting curve on the XPS spectrum around the VBM (Figure 4(b)). The AlN NMs coated with an ultrathin ALD deposited SiO_2 or Al_2O_3 were also measured to investigate the effect of UO coating on the surface charge. The uncertainty of the measurement was estimated to be 0.2 eV. [81, 82] As shown in Figure 4(c), the bare Al-polar surface of the AlN NM sample has a larger $q\phi_S$ than the bare N-polar surface, indicating that there is more positive charge on the bare Al-polar surface than the bare N-polar surface. If only considering the polarization charge, under the tensile strain, the spontaneous polarization and piezoelectric polarization would be parallel to each other. [83] This means that more negative charge is expected on the Al-polar surface than N-polar according to the

This article is protected by copyright. All rights reserved.

polarization of AlN, which is contrary to what we observed through XPS. Therefore, one reasonable speculation is that the strong Fermi level pinning effect from the surface states, which has been observed in nitride materials through XPS measurements, [79, 84] has dominated the polarization effect, and more positive charge is observed on the Al-polar surface. In addition, the deposition of 5 cycles of ALD-SiO_2 and post deposition annealing (PDA) in N_2 ambient at 350 °C for 5 min by RTA generates more positive charge to the Al-polar surface. On the other hand, ALD-Al_2O_3 tends not to have much impact on the surface charge of AlN NMs. It is expected that an optimized ultrathin interfacial dielectric layer can potentially reduce the interface state density, [4] thus promising for AlN-based heterostructure vertical devices.

3. Conclusion

We have successfully created, transferred, and characterized single-crystalline AlN NMs. The AlN NM crystalline quality has been retained after the creation and transfer-printing processes. The crystalline quality has been characterized and confirmed by a broad range of techniques. The single-crystalline pure wurtzite phase c-axis orientation has been confirmed by STEM and XRD. The piezoelectric response has been confirmed by PFM measurements. The energy band-bending properties of both Al-polar and N-polar surfaces have been characterized by detailed XPS measurements. The excellent material, electronic, and piezoelectric properties obtained from the AlN NMs collectively are expected to enable a new range of AlN-based heterogeneous electronics and optoelectronics on both rigid and flexible foreign substrates in the future.

4. Experimental Section

Nanomembrane fabrication and transfer: The 50 nm/400 nm unintentionally doped (UID) AlN (0001)/Al (111) epi layer was grown on the Si (111) substrate via a Veeco

This article is protected by copyright. All rights reserved.

GENxplor MBE system. The thickness of the AlN epi layer has been confirmed by STEM (Figure S5). Detailed study of the growth technique will be reported separately. In brief, the single crystalline Al (111) of 400 nm was firstly grown on a Si (111) substrate. On top of the epitaxial Al (111) layer, a single-crystalline wurtzite AlN of 50 nm was grown. The finished AlN epi layer is Al-polar.

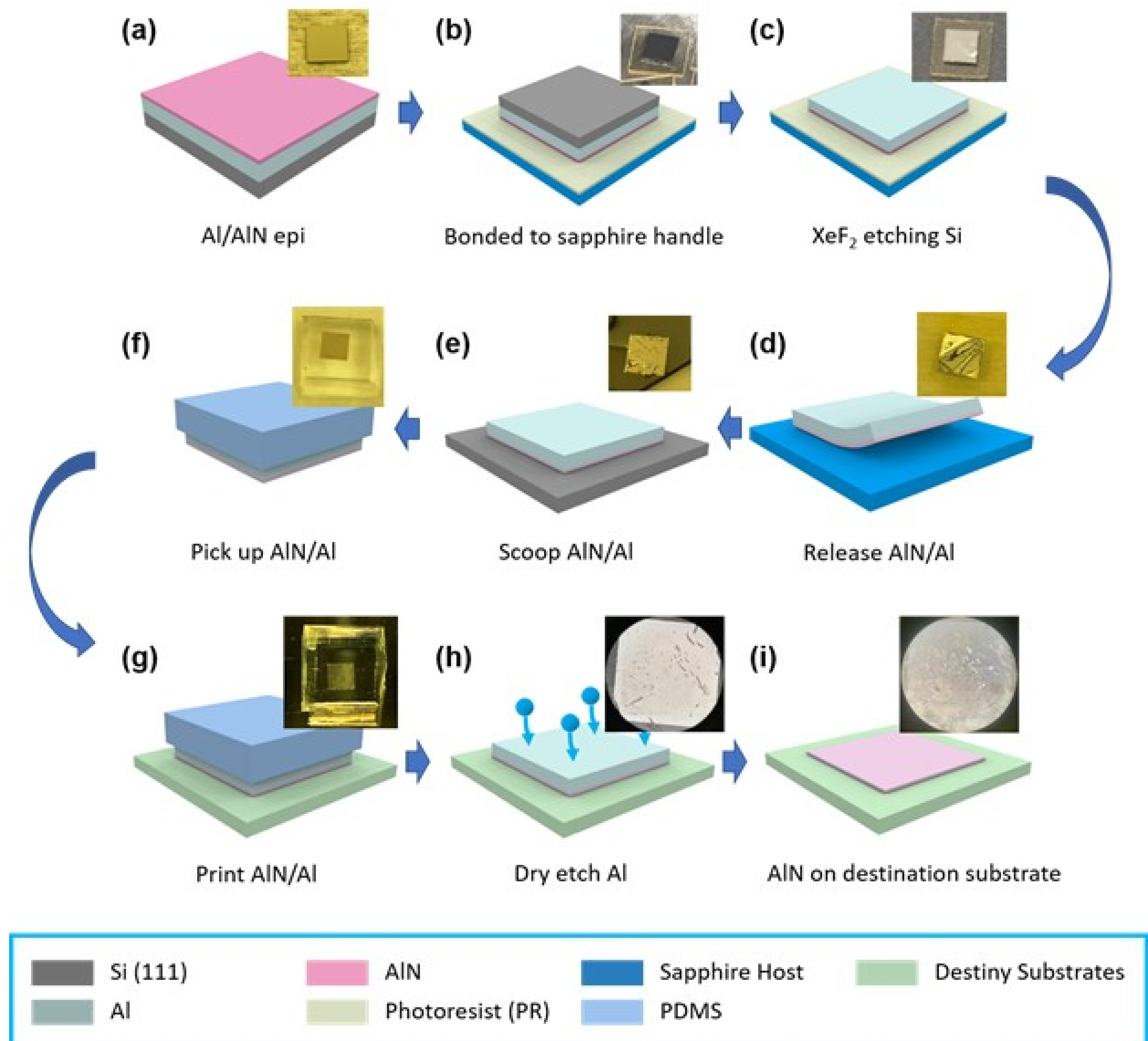

Figure 5. Fabrication and transfer-printing process of the AlN NM. (a) Structure of the AlN/Al/Si epi with the photo of the diced epi sample. (b) AlN/Al/Si epi is flipped and bonded to the sapphire handle with the photo of the bonded sample. (c) Si substrate is removed by XeF_2 dry etching with the photo of the bonded sample after etching. (d) AlN/Al NM is

This article is protected by copyright. All rights reserved.

released by undercutting photoresist with the photo of the AlN/Al NM floating in acetone solution and (e) scooped by a Si handle wafer with the photo of the AlN/Al NM on the Si handle wafer. (f) The AlN/Al NM is picked up by a PDMS stamp with the photo of the AlN/Al NM on the PDMS stamp, and (g) then transfer-printed to a destiny substrate with the photo of the AlN/Al NM being printed by the PDMS stamp. (h-i) The free-standing AlN NM is finalized by dry etching of the Al layer with the photos of the AlN/Al NM (h) before and (i) after etching. The final thickness of the AlN NM is only 30 nm resulting from over-etching in the Al etching step.

After fabricating the epitaxial wafer of AlN, it was first diced into 4×4 mm^2 pieces (Fig 1(a)). To release the AlN NMs from the epitaxial wafer, a standard semiconductor cleaning process was first performed on the AlN/Al/Si epi using acetone, IPA, and DI water sequentially in the ultrasonic bath for 10 min each and then dried using N_2. The epi wafer was (with AlN facing) attached to a temporary sapphire substrate, which had been spin-coated by the photoresist (PR) AZ5214 (Figure 5(b)). The whole stack of Si/Al/AlN/PR/sapphire (from top to bottom) was then baked together at 120 °C for 15 min on a hotplate. The Si was selectively removed by the SPTS Xactix E1 XeF_2 etcher, with the NM form of AlN/Al left on the temporary sapphire substrate (Figure 5(c)). Further, the remaining stack of AlN/Al/PR/sapphire was soaked into acetone to undercut the PR layer and release the AlN/Al NM from the sapphire substrate (Figure 5(d)). It is noteworthy that the freestanding AlN/Al NMs could curl down, as AlN layer is inside and Al layer is outside, in the acetone due to strain originated from the lattice mismatch between AlN and Al when released from the host substrate. To flatten the AlN/Al NM, acetone was gradually drained and meanwhile deionized (DI) water was gradually added. The DI water, having stronger surface tension than acetone, [85-87] helped to unfold the curled AlN/Al NMs and make it float on the liquid surface. As a next step, a Si substrate was used to “scoop” the floating AlN/Al NMs from the

This article is protected by copyright. All rights reserved.

DI water (Figure 5(e)).[10] Further, the DI water residues were dried out using N_2. Moving forward, the AlN/Al NMs, sitting on the Si substrate, was picked up by a polydimethylsiloxane (PDMS) stamp (shown in Figure 5(f)) and was transfer-printed onto the destination substrate (e.g. Si, and sapphire) as shown in Figure 5(g). It is noted that the existence of the Al (111) interlayer helps “soften” the rigidity of AlN NM, which makes the PDMS-assisted transfer process feasible as the Al/AlN NM becomes more compliant to the substrate. The PDMS stamp is also surface-textured, rather than flat, to reduce its surface adhesion to the NM to make the transfer possible. Finally, the free-standing single-crystalline AlN NM was obtained by removing the top 400 nm-thick Al layer using Plasma-Therm reactive ion etching (RIE) (Figure 5(g) and 1(i)). For the etching process, a mixture of BCl_3, Cl_2, and Ar gases was used which has high selectivity between Al and AlN layers. XPS survey spectra were measured before and after the RIE etching to confirm removal of the Al layer (Figure S2). The remaining AlN NM thickness after the Al layer etching is 30 nm.

Compared with deposition of AlN thin films, the transfer-printing method allows us to inherit the high single-crystalline quality of AlN grown using state-of-the-art MBE technique regardless of the final host substrates, which is beneficial to applications such as AlN-based flexible electronics [83] and III-V/Si integration.[88] In addition, via substrate flipping we utilize the top surface of the as-grown epi wafer as the contact surface, which has better crystal quality than the bottom surface of AlN due to the nucleation at the bottom surface. In comparison to the exfoliation method of the remote epitaxy growth, our method does not require the deposition of a stressor layer or handling layer on top of the as-grown NM.[89] Therefore, this clean and smooth contact surface provides us the possibility to create a firmly bonded interface with the substrate.

Additionally, such MBE-grown AlN thin films have good scaling and doping controllability. In our current experiments, the thickness of the as-grown AlN film can be

This article is protected by copyright. All rights reserved.

controlled from even monolayer up to 200 nm that is crack-free and with a smooth surface. Furthermore, to develop high-performance transistors that are based on such an AlN membrane, the doping profile of the AlN film can be precisely modified by introducing efficient dopants, such as beryllium (Be) and silicon (Si). [90, 91]

Topography and structural measurements: Scanning electron microscope (SEM) images (Figure 1(a)-(c)) of the transferred AlN NM were taken by Zeiss LEO 1530 field emission SEM system. The AlN NM was transferred to a patterned Si substrate that has an array of hexagon shaped pillars. XRD 2theta-omega spectra (Figure 1(e)) were measured on both as-grown and transferred AlN samples by a Malvern Panalytical Empyrean X-ray diffractometer with a Cu K-α X-ray source. Raman spectra (Figure 1(f)) were obtained from both as-grown and transferred AlN samples by a Horiba LabRAM HR Evolution Raman spectrometer using a 532-nm laser. Considering the fact that the AlN NM is only 54 nm thick, the confocal hole size of the spectrometer and the acquisition time were set to be 25 μm and 20 min, respectively, to increase the axial resolution and the layer discrimination while maintaining a moderate signal-to-noise ratio. The electron backscatter diffraction (EBSD) map (Figure 1(g)) was collected on the transferred AlN NM at 20 kV and 10 nA with a Zeiss Merlin High-resolution SEM system equipped with an EBSD detector. AFM images was taken by a Bruker Dimension Icon AFM system.

Microstructural measurements: STEM specimen was prepared by a Thermo Fisher Scientific Helios G4 UXe focus ion beam (FIB). High-angle annular dark-field and annular bright-field STEM (HAADF-STEM and ABF-STEM) images were collected using a Cs corrected JEOL 3100R05 microscope operated at 300 kV.

Piezoresponse force microscopy measurements: PFM measurements were performed using a Bruker Dimension Icon AFM system. In this measurement, an AFM with a conductive probe was used to create a vertical electric field through the sample material by

This article is protected by copyright. All rights reserved.

applying a driving voltage between the tip and substrate while the AFM operated in contact mode, as shown schematically in Figure S6. In the presence of piezoelectricity in the sample, the AFM tip would be deflected by the expansion and contraction of the material induced by the converse piezoelectric effect. A lock-in amplifier was used to detect the amplitude and phase of the response. The effective piezoelectric response, $d_{33,\mathrm{eff}}$, was then obtained via an analysis procedure described in detail elsewhere. [67, 68] Because of the substantial difference in elastic modulus between the AlN NM and Si (100) substrate, it was also necessary to account for deformation of the Si substrate beneath the AlN NM, which would alter the surface deflection measured in PFM. [70] The true piezoelectric coefficient d_{33} of the AlN layer could then be determined based on the analysis given in the reference, [70] and was found to be substantially larger than $d_{33,\mathrm{eff}}$.

Valance band maximum measurements: The XPS characterizations were performed on as-grown and transferred AlN samples with a Thermo Scientific K Alpha X-ray Photoelectron Spectrometer with Al K_{α} X-ray source (hv = 1486.6 eV). The detailed setup of the XPS instrumental parameters has been reported in our previous works. [81, 82]

Supporting Information

Supporting Information is available from the Wiley Online Library or from the author.

Acknowledgement

The work was supported by the Defense Advanced Research Projects Agency (DARPA) H2 program under the grant HR00112190107 and partially by Air Force Office of Scientific Research (AFOSR) under grant FA9550-21-1-0081. Part of this work was supported by the National Science Foundation (NSF) under award No. DMR-1905287.

This article is protected by copyright. All rights reserved.

References

1. M. A. Meitl, Z.-T. Zhu, V. Kumar, K. J. Lee, X. Feng, Y. Y. Huang, I. Adesida, R. G. Nuzzo, and J. A. Rogers, *Nature Materials*, 2006, **5**(1), 33.
2. J. Rogers, M. Lagally, and R. Nuzzo, *Nature*, 2011, **477**(7362), 45-53.
3. A. Carlson, A. M. Bowen, Y. Huang, R. G. Nuzzo, and J. A. Rogers, *Advanced Materials*, 2012, **24**(39), 5284-5318.
4. D. Liu, S. J. Cho, J.-H. Seo, K. Kim, M. Kim, J. Shi, X. Yin, W. Choi, C. Zhang, J. Kim, M. A. Baboli, J. Park, J. Bong, I.-K. Lee, J. Gong, S. Mikael, J. H. Ryu, P. K. Mohseni, X. Li, S. Gong, X. Wang, and Z. Ma, *arXiv preprint arXiv:1812.10225*, 2018.
5. D.-Y. Khang, H. Jiang, Y. Huang, and J. A. Rogers, *Science*, 2006, **311**(5758), 208-212.
6. Y. Sun, W. M. Choi, H. Jiang, Y. Y. Huang, and J. A. Rogers, *Nature Nanotechnology*, 2006, **1**(3), 201-207.
7. J.-H. Ahn, H.-S. Kim, K. J. Lee, S. Jeon, S. J. Kang, Y. Sun, R. G. Nuzzo, and J. A. Rogers, *Science*, 2006, **314**(5806), 1754-1757.
8. D.-H. Kim, J.-H. Ahn, W. M. Choi, H.-S. Kim, T.-H. Kim, J. Song, Y. Y. Huang, Z. Liu, C. Lu, and J. A. Rogers, *Science*, 2008, **320**(5875), 507-511.
9. J. Yoon, A. J. Baca, S.-I. Park, P. Elvikis, J. B. Geddes, L. Li, R. H. Kim, J. Xiao, S. Wang, and T.-H. Kim, *Nature Materials*, 2008, **7**(11), 907-915.
10. A. M. Kiefer, D. M. Paskiewicz, A. M. Clausen, W. R. Buchwald, R. A. Soref, and M. G. Lagally, *ACS Nano*, 2011, **5**(2), 1179-1189.
11. J. H. Seo, T. Y. Oh, J. Park, W. Zhou, B. K. Ju, and Z. Ma, *Advanced Functional Materials*, 2013, **23**(27), 3398-3403.

Author Manuscript

This article is protected by copyright. All rights reserved.

Author Manuscript

12. S.-K. Kang, R. K. Murphy, S.-W. Hwang, S. M. Lee, D. V. Harburg, N. A. Krueger, J. Shin, P. Gamble, H. Cheng, and S. Yu, *Nature*, 2016, **530**(7588), 71-76.

13. J.-H. Seo, K. Zhang, M. Kim, W. Zhou, and Z. Ma, *NPJ Flexible Electronics*, 2017, **1**(1), 1-7.

14. D. Liu, S. J. Cho, J. Park, J.-H. Seo, R. Dalmau, D. Zhao, K. Kim, J. Gong, M. Kim, and I.-K. Lee, *Applied Physics Letters*, 2018, **112**(8), 081101.

15. D. Liu, S. J. Cho, J. Park, J. Gong, J.-H. Seo, R. Dalmau, D. Zhao, K. Kim, M. Kim, and A. R. Kalapala, *Applied Physics Letters*, 2018, **113**(1), 011111.

16. Y. Liu, L. Wang, L. Wang, X. Wu, Z. Hao, J. Yu, Y. Luo, C. Sun, Y. Han, and B. Xiong, *Semiconductor Science and Technology*, 2019, **34**(10), 105023.

17. Y. Zheng, M. N. Hasan, and J. H. Seo, *Advanced Materials Technologies*, 2021, **6**(6), 2100254.

18. K. Kim, J. Jang, and H. Kim, *Results in Physics*, 2021, **25**, 104279.

19. C. Chen, C. Li, S. Min, Q. Guo, Z. Xia, D. Liu, Z. Ma, and F. Xia, *Nano Letters*, 2021, **21**(19), 8385-8392.

20. M. N. Hasan, Y. Zheng, J. Lai, E. Swinnich, O. G. Licata, M. A. Baboli, B. Mazumder, P. K. Mohseni, and J. H. Seo, *Advanced Materials Interfaces*, 2022, **9**(13), 2101531.

21. Z. Xia, H. Song, M. Kim, M. Zhou, T.-H. Chang, D. Liu, X. Yin, K. Xiong, H. Mi, and X. Wang, *Science Advances*, 2017, **3**(7), e1602783.

22. S.-I. Park, Y. Xiong, R.-H. Kim, P. Elvikis, M. Meitl, D.-H. Kim, J. Wu, J. Yoon, C.-J. Yu, and Z. Liu, *Science*, 2009, **325**(5943), 977-981.

23. J. Yoon, S. Jo, I. S. Chun, I. Jung, H.-S. Kim, M. Meitl, E. Menard, X. Li, J. J. Coleman, and U. Paik, *Nature*, 2010, **465**(7296), 329-333.

This article is protected by copyright. All rights reserved.

24. J. Lee, J. Wu, M. Shi, J. Yoon, S. I. Park, M. Li, Z. Liu, Y. Huang, and J. A. Rogers, *Advanced Materials*, 2011, **23**(8), 986-991.

25. K. Xiong, H. Mi, T. H. Chang, D. Liu, Z. Xia, M. Y. Wu, X. Yin, S. Gong, W. Zhou, and J. C. Shin, *Energy Science & Engineering*, 2018, **6**(1), 47-55.

26. S. J. Cho, D. Liu, A. Hardy, J. Kim, J. Gong, C. J. Herrera-Rodriguez, E. Swinnich, X. Konstantinou, G.-Y. Oh, and D. G. Kim, *AIP Advances*, 2020, **10**(12), 125226.

27. S. H. Park, G. Yuan, D. Chen, K. Xiong, J. Song, B. Leung, and J. Han, *Nano Letters*, 2014, **14**(8), 4293-4298.

28. T.-H. Chang, K. Xiong, S. H. Park, G. Yuan, Z. Ma, and J. Han, *Scientific Reports*, 2017, **7**(1), 1-9.

29. Y.-Y. Zhang, Y.-X. Zheng, J.-Y. Lai, J.-H. Seo, K. H. Lee, C. S. Tan, S. An, S.-H. Shin, B. Son, and M. Kim, *ACS Nano*, 2021, **15**(5), 8386-8396.

30. Y. Y. Zhang, S. An, Y. Zheng, J. Lai, J. H. Seo, K. H. Lee, and M. Kim, *Advanced Electronic Materials*, 2022, **8**(2), 2100652.

31. M. Kim, J.-H. Seo, D. Zhao, S.-C. Liu, K. Kim, K. Lim, W. Zhou, E. Waks, and Z. Ma, *Journal of Materials Chemistry C*, 2017, **5**(2), 264-268.

32. E. Swinnich, M. N. Hasan, K. Zeng, Y. Dove, U. Singisetti, B. Mazumder, and J. H. Seo, *Advanced Electronic Materials*, 2019, **5**(3), 1800714.

33. Y. Zheng, E. Swinnich, and J.-H. Seo, *ECS Journal of Solid State Science and Technology*, 2020, **9**(5), 055007.

34. J. Lai, M. N. Hasan, E. Swinnich, Z. Tang, S.-H. Shin, M. Kim, P. Zhang, and J.-H. Seo, *Journal of Materials Chemistry C*, 2020, **8**(42), 14732-14739.

35. Y. Zheng, Z. Feng, A. A. U. Bhuiyan, L. Meng, S. Dhole, Q. Jia, H. Zhao, and J.-H. Seo, *Journal of Materials Chemistry C*, 2021, **9**(19), 6180-6186.

Author Manuscript

This article is protected by copyright. All rights reserved.

36. M. Feneberg, R. A. Leute, B. Neuschl, K. Thonke, and M. Bickermann, *Physical Review B*, 2010, **82**(7), 075208.

37. J. Tsao, S. Chowdhury, M. Hollis, D. Jena, N. Johnson, K. Jones, R. Kaplar, S. Rajan, C. Van de Walle, and E. Bellotti, *Advanced Electronic Materials*, 2018, **4**(1), 1600501.

38. G. A. Slack, R. A. Tanzilli, R. Pohl, and J. Vandersande, *Journal of Physics and Chemistry of Solids*, 1987, **48**(7), 641-647.

39. J. Li, Z. Fan, R. Dahal, M. Nakarmi, J. Lin, and H. Jiang, *Applied Physics Letters*, 2006, **89**(21), 213510.

40. T. Li, L. Long, Z. Hu, R. Wan, X. Gong, L. Zhang, Y. Yuan, J. Yan, W. Zhu, and L. Wang, *Optics Letters*, 2020, **45**(12), 3325-3328.

41. Y. Irokawa, E. A. G. Víllora, and K. Shimamura, *Japanese Journal of Applied Physics*, 2012, **51**(4R), 040206.

42. H. Fu, I. Baranowski, X. Huang, H. Chen, Z. Lu, J. Montes, X. Zhang, and Y. Zhao, *IEEE Electron Device Letters*, 2017, **38**(9), 1286-1289.

43. K. Tonisch, V. Cimalla, C. Foerster, H. Romanus, O. Ambacher, and D. Dontsov, *Sensors and Actuators A: Physical*, 2006, **132**(2), 658-663.

44. M. D. Williams, B. A. Griffin, T. N. Reagan, J. R. Underbrink, and M. Sheplak, *Journal of Microelectromechanical Systems*, 2012, **21**(2), 270-283.

45. N. Jackson, L. Keeney, and A. Mathewson, *Smart Materials and Structures*, 2013, **22**(11), 115033.

46. V. M. Mastronardi, F. Guido, M. Amato, M. De Vittorio, and S. Petroni, *Microelectronic Engineering*, 2014, **121**, 59-63.

47. X. Yang, J. Liang, Y. Jiang, X. Chen, H. Zhang, M. Zhang, and W. Pang, *IEEE Electron Device Letters*, 2017, **38**(8), 1125-1127.

Author Manuscript

This article is protected by copyright. All rights reserved.

48. A. Gao, K. Liu, J. Liang, and T. Wu, *Microsystems & Nanoengineering*, 2020, **6**(1), 1-11.

49. J. Simon, V. Protasenko, C. Lian, H. Xing, and D. Jena, *Science*, 2010, **327**(5961), 60-64.

50. Y. Mei, D. J. Thurmer, C. Deneke, S. Kiravittaya, Y.-F. Chen, A. Dadgar, F. Bertram, B. Bastek, A. Krost, and J. r. Christen, *ACS Nano*, 2009, **3**(7), 1663-1668.

51. J. Yang, Y. Wang, L. Wang, Z. Tian, Z. Di, and Y. Mei, *Journal of Semiconductors*, 2020, **41**(4), 042601.

52. A. Khandelwal, N. Athreya, M. Q. Tu, L. L. Janavicius, Z. Yang, O. Milenkovic, J.-P. Leburton, C. M. Schroeder, and X. Li, *Microsystems & Nanoengineering*, 2022, **8**(1), 1-12.

53. A. Khandelwal, Z. Ren, S. Namiki, Z. Yang, N. Choudhary, C. Li, P. Wang, Z. Mi, and X. Li, *ACS Applied Materials & Interfaces*, 2022.

54. E. Azrak, L. G. Michaud, A. Reinhardt, S. Tardif, M. Bousquet, N. Vaxelaire, J. Eymery, F. Fournel, and P. Montmeat, *ECS Journal of Solid State Science and Technology*, 2021, **10**(6), 064001.

55. Y. Jia, H. Wu, J. Zhao, H. Guo, Y. Zeng, B. Wang, C. Zhang, Y. Zhang, J. Ning, and J. Zhang, *CrystEngComm*, 2021, **23**(42), 7406-7411.

56. Z. Shi, X. Lu, X. Tang, D. Wang, Z. Cong, X. Ma, and Y. Hao, *Applied Surface Science*, 2022, **585**, 152378.

57. P. Scherrer: 'Bestimmung der inneren Struktur und der Größe von Kolloidteilchen mittels Röntgenstrahlen', in 'Kolloidchemie Ein Lehrbuch', 387-409; 1912, Springer.

58. A. Patterson, *Physical Review*, 1939, **56**(10), 978.

59. T. Prokofyeva, M. Seon, J. Vanbuskirk, M. Holtz, S. Nikishin, N. Faleev, H. Temkin, and S. Zollner, *Physical Review B*, 2001, **63**(12), 125313.

This article is protected by copyright. All rights reserved.

Author Manuscript

60. V. Lughi and D. R. Clarke, *Applied Physics Letters*, 2006, **89**(24), 241911.

61. M. Morita, T. Ohmi, E. Hasegawa, M. Kawakami, and M. Ohwada, *Journal of Applied Physics*, 1990, **68**(3), 1272-1281.

62. M. Kazan, E. Moussaed, R. Nader, and P. Masri, *Physica Status Solidi C*, 2007, **4**(1), 204-207.

63. D. Zagorac, J. Zagorac, M. Djukic, D. Jordanov, and B. Matović, *Theoretical and Applied Fracture Mechanics*, 2019, **103**, 102289.

64. W. Yim and R. Paff, *Journal of Applied Physics*, 1974, **45**(3), 1456-1457.

65. P. Wang, Y. Yuan, C. Zhao, X. Wang, X. Zheng, X. Rong, T. Wang, B. Sheng, Q. Wang, and Y. Zhang, *Nano Letters*, 2016, **16**(2), 1328-1334.

66. P. Wang, D. Wang, S. Mondal, Y. Wu, T. Ma, and Z. Mi, *ACS Applied Materials & Interfaces*, 2022, **14**(13), 15747-15755.

67. C. J. Brennan, R. Ghosh, K. Koul, S. K. Banerjee, N. Lu, and E. T. Yu, *Nano Letters*, 2017, **17**(9), 5464-5471.

68. C. J. Brennan, K. Koul, N. Lu, and E. T. Yu, *Applied Physics Letters*, 2020, **116**(5), 053101.

69. B. J. Rodriguez, A. Gruverman, A. Kingon, and R. Nemanich, *Journal of Crystal Growth*, 2002, **246**(3-4), 252-258.

70. J.-H. Li, L. Chen, V. Nagarajan, R. Ramesh, and A. Roytburd, *Applied Physics Letters*, 2004, **84**(14), 2626-2628.

71. J. Wortman and R. Evans, *Journal of Applied Physics*, 1965, **36**(1), 153-156.

72. A. Wright, *Journal of Applied Physics*, 1997, **82**(6), 2833-2839.

73. E. Österlund, J. Kinnunen, V. Rontu, A. Torkkeli, and M. Paulasto-Kröckel, *Journal of Alloys and Compounds*, 2019, **772**, 306-313.

74. I. Guy, S. Muensit, and E. Goldys, *Applied Physics Letters*, 1999, **75**(26), 4133-4135.

Author Manuscript

This article is protected by copyright. All rights reserved.

Author Manuscript

75. C. Lueng, H. L. Chan, C. Surya, and C. Choy, *Journal of Applied Physics*, 2000, **88**(9), 5360-5363.

76. F. Bernardini and V. Fiorentini, *Applied Physics Letters*, 2002, **80**(22), 4145-4147.

77. P. Wang, D. A. Laleyan, A. Pandey, Y. Sun, and Z. Mi, *Applied Physics Letters*, 2020, **116**(15), 151903.

78. P. Wang, B. Wang, D. A. Laleyan, A. Pandey, Y. Wu, Y. Sun, X. Liu, Z. Deng, E. Kioupakis, and Z. Mi, *Applied Physics Letters*, 2021, **118**(3), 032102.

79. P. Reddy, I. Bryan, Z. Bryan, W. Guo, L. Hussey, R. Collazo, and Z. Sitar, *Journal of Applied Physics*, 2014, **116**(12), 123701.

80. D. A. Shirley, *Physical Review B*, 1972, **5**(12), 4709.

81. J. Gong, K. Lu, J. Kim, T. Ng, D. Kim, J. Zhou, D. Liu, J. Kim, B. S. Ooi, and Z. Ma, *Japanese Journal of Applied Physics*, 2021, **61**(1), 011003.

82. J. Gong, Z. Zheng, D. Vincent, J. Zhou, J. Kim, D. Kim, T. K. Ng, B. S. Ooi, K. J. Chen, and Z. Ma, *Journal of Applied Physics*, 2022, **132**(13), 135302.

83. C. Fei, X. Liu, B. Zhu, D. Li, X. Yang, Y. Yang, and Q. Zhou, *Nano Energy*, 2018, **51**, 146-161.

84. Y. Jia, J. S. Wallace, E. Echeverria, J. A. Gardella Jr, and U. Singisetti, *Physica Status Solidi (B)*, 2017, **254**(8), 1600681.

85. K. S. Howard and R. McAllister, *AIChE Journal*, 1957, **3**(3), 325-329.

86. S. Enders, H. Kahl, and J. Winkelmann, *Journal of Chemical & Engineering Data*, 2007, **52**(3), 1072-1079.

87. N. Wu, X. Li, S. Liu, M. Zhang, and S. Ouyang, *Applied Sciences*, 2019, **9**(6), 1235.

88. G. Roelkens, J. Van Campenhout, J. Brouckaert, D. Van Thourhout, R. Baets, P. R. Romeo, P. Regreny, A. Kazmierczak, C. Seassal, and X. Letartre, *Materials Today*, 2007, **10**(7-8), 36-43.

This article is protected by copyright. All rights reserved.

89. H. Kim, C. S. Chang, S. Lee, J. Jiang, J. Jeong, M. Park, Y. Meng, J. Ji, Y. Kwon, and X. Sun, *Nature Reviews Methods Primers*, 2022, **2**(1), 1-21.

90. H. Ahmad, J. Lindemuth, Z. Engel, C. M. Matthews, T. M. McCrone, and W. A. Doolittle, *Advanced Materials*, 2021, **33**(42), 2104497.

91. H. Ahmad, Z. Engel, C. M. Matthews, S. Lee, and W. A. Doolittle, *Journal of Applied Physics*, 2022, **131**(17), 175701.

TOC

A novel method to fabricate and transfer-print single crystalline AlN nanomembranes to several foreign substrates is demonstrated and no degradation of the AlN nanomembranes is observed by a range of characterization techniques through the whole process, which shows a promising potential for future applications in flexible electronics and heterogeneous integration.

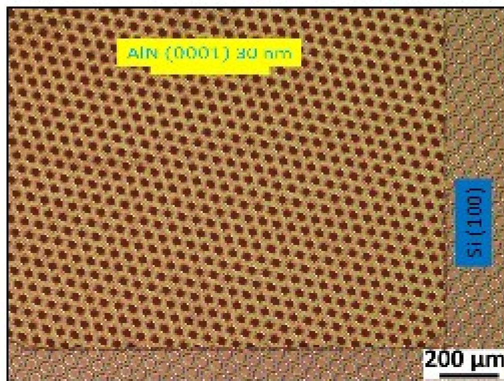

Author Manuscript

This article is protected by copyright. All rights reserved.